The Astrophysical Journal, 773:162 (8pp), 2013 August 20 doi:10.1088/0004-637X/773/2/162
© 2013. The American Astronomical Society. All rights reserved. Printed in the U.S.A.

ANALYSIS OF THE SIMULTANEOUS ROTATION AND NON-RADIAL PROPAGATION OF AN ERUPTIVE FILAMENT

Yi Bi[1], Yunchun Jiang[1], Jiayan Yang[1,2], Ruisheng Zheng[1], Junchao Hong[1,3], Haidong Li[1], Dan Yang[1,3], and Bo Yang[1,3]
[1] Yunnan Astronomical Observatory, Chinese Academy of Sciences, P.O. Box 110, Kunming 650011, China; biyi@ynao.ac.cn
[2] Key Laboratory for the Structure and Evolution of Celestial Objects, Chinese Academy of Sciences, Kunming 650011, China
[3] Graduate School of Chinese Academy of Sciences, Beijing 100049, China
Received 2012 September 28; accepted 2013 June 12; published 2013 August 6

ABSTRACT

The rotation of eruptive filaments is not only related to the kink instability occurring in the solar corona but also may result from the interaction between the large-scale magnetic field and the eruptions themselves. This interaction could likewise make the filament deflect in the radial direction. By means of data obtained by the Atmospheric Imaging Assembly on board the *Solar Dynamics Observatory* and observations from the *Solar Terrestrial Relations Observatory*, we study an eruptive filament showing both rotation and non-radial motion. The consequence of the three-dimensional reconstruction of the filament axis indicates that a significant rotation was simultaneous with the severe deflection in the latitude during the eruption. In combination with the results of a derived coronal magnetic configuration, our observations suggested that the non-radial motion resulted from the interaction between the eruption and an overlying pseudostreamer. Moreover, we find that the deflection of the eruption is asymmetric, with its eastern segment being dragged more significantly than its western one. Therefore, we suggested that the action of the asymmetric deflection is possibly an alternative mechanism for the rotation of the eruptive filament.

Key words: Sun: filaments, prominences – Sun: magnetic topology

Online-only material: color figures

1. INTRODUCTION

The eruption of a solar filament is the consequence of a sudden destabilization of a part of the coronal magnetic field. The onset of the eruption is often preceded by a relatively slow rising motion (e.g., Zhang et al. 2001, 2004; Cheng et al. 2010; Sterling et al. 2011). This gradual evolution is frequently triggered by the evolution of the magnetic field in the vicinity of the photospheric inversion line, such as a new flux emerging, the progressive dispersion or cancellation of the flux, or buildup of a very shear field. After the filament slowly rises, it suddenly erupts; this eruption is either driven by the torus instability or results from a loss of equilibrium (Forbes & Isenberg 1991; Kliem Török 2006). Démoulin & Aulanier (2010) suggested that the two mechanisms were actually different views of the same physical mechanism. The eruption trigger mechanism is responsible for these early motions, while the driving mechanism is responsible for the rapid acceleration of the filament.

The rotation of the eruptive filament is an important topic in solar physics. On the one hand, filament eruptions represent the evolution of the coronal mass ejections (CMEs) in the low corona, and the magnetic orientation of the CME is one of the key issues in space weather research. On the other hand, the rotation of the filament has been widely accepted as the "footprint" of the occurrence of kink instability in an eruption (Hood & Priest 1979; Hood 1992; Kliem et al. 2004; Fan 2005; Török et al. 2010). When the twist of the magnetic field associated with the filament exceeds a critical value, it becomes kink instability and the filament undergoes a writhe motion (e.g., Rust & LaBonte 2005; Zhou et al. 2006; Green et al. 2007; Liu et al. 2008). The writhe, which can be thought of as the rotation causing the helicity of the flux-rope axis itself when a flux rope experiences a kinking motion, is converted from the twist of the field required by the magnetic helicity conservation (Berger & Prior 2006). Simulations by Török & Kliem (2005) showed that the kink instability eruption would be confined if the overlying magnetic field of the filament were strong enough and decreased slowly with height. Their numerical research explains the observation investigated by Ji et al. (2003), who found an eruptive filament with a kink motion that failed to evolve into CMEs (Liu 2008; Shen et al. 2011b). Kliem et al. (2012) suggested that the helical kink instability lifts the flux rope associated with the filament into the torus-unstable range of heights, from where the filament is accelerated further upward by torus instability.

The interaction between the eruptive flux rope and the associated surrounding magnetic field could also play a leading role in the rotation of the filament. First, Isenberg & Forbes (2007) found that the Lorentz force induced by the current in a filament and the shear magnetic field can rotate the filament. In their study, this force appears immediately when a lifting flux rope is not parallel to the external shear field component pointing along the rope. As suggested by Kliem et al. (2012), however, the rotation due to kink instability tends to act predominantly low in the corona, while the rotation by the shear field tends to be distributed across a wider height range. Considering that the surrounding field is non-potential, Cohen et al. (2010) suggested that the rotation resulted from the reconnection of the core flux rope and the neighboring field during the initial stage of CME expansion (also see Jacobs et al. 2009; Lugaz et al. 2011).

A similar interaction may also affect the direction of propagation of the eruption: Filippov et al. (2001) proposed that the guiding action of the coronal magnetic field deflects the eruption. The deflection of this CME at an early stage may be caused by a nonuniform distribution of the background magnetic field energy density, and the CME will tend to propagate to the region with lower magnetic energy density (Shen et al. 2011a). Focusing on the flare in an outer flank of the base of a streamer,

Bemporad et al. (2005) found that the associated eruption was far offset laterally along the streamer. Moore & Sterling (2007) identified an eruption guided by a streamer as an over-and-out CME. Jiang et al. (2009) investigated the evolution of a non-radial filament eruption and identified it as the appearance of an over-and-out CME in the inner corona. Panasenco et al. (2011) observed that the three eruptive filaments propagated away from the neighboring coronal hole, and they suggested that the non-radial motion is related to global magnetic configuration force imbalances. In the simulation provided by Zuccarello et al. (2012), even a filament originating outside a streamer could deflect and finally enter the streamer, owing to an imbalance in the magnetic pressure and tension force. In their case, the filament initially located under the southern side arched in a pseudostreamer (Wang et al. 2007), and the strong deflection of the filament was initially caused by the reconnection between the expanding southern arcade and the open field to the north of it. Similarly, Sun et al. (2012) recently inferred that the non-radial motion of an eruption was facilitated by the reconnection taking place near the coronal null point in a quadrupolar system.

The *Solar Terrestrial Relations Observatory* (*STEREO*) has provided extreme ultraviolet (EUV) observations from different views with its twin telescopes, which are located in front of and behind the earth, respectively. Including observations from the *Solar Dynamics Observatory* (*SDO*), the EUV images from three different views are available at the same time. Images from different views allow the reconstruction of the actual three-dimensional (3D) structure of a solar filament without any limitation due to projection effects. Several studies have identified the rotation of filaments from the 3D construction (Bemporad et al. 2011; Thompson et al. 2012; Joshi & Srivastava 2011). In these studies, however, there was always one view from which the pre-eruptive filament was located behind the limb, and in that case, it is difficult to know when the filament started to rotate in these eruptions.

In this study, we present the eruption of a filament located on the solar disk from the views of both *SDO* and *STEREO-B*. Section 2 gives the details of the observation. In Section 3, we identified the rotation and deflection of the filament in the eruption through the two views of the observations. We discuss the implications of the observations in Section 4.

2. OBSERVATIONS

Our primary data source is full-disk EUV images from the Atmospheric Imaging Assembly (AIA; Boerner et al. 2012) aboard the *SDO*. The AIA takes EUV images with a pixel size of 0.″6 and 12 s cadence. To study the topology of the eruptive filament, we focus on the 304 Å (He II; $\log T = 4.7$) and 211 Å (Fe XIV; $\log T = 6.3$) images. To detail the post-event flaring loop, we adopt the 94 Å (Fe XVIII; $\log T = 6.8$) images. The Helioseismic and Magnetic Imager (HMI; Wachter et al. 2012) provides full-disk magnetograms observed in the Fe I 6173 Å absorption line, with a spatial sampling of 0.″5 pixel^{-1}, 45 s cadence, and a noise level of approximately 10 G.

On 2011 April 27, the *STEREO-B* spacecraft was about 94° behind the Earth. The filament was located in the eastern hemisphere as viewed by *SDO* and in the western hemisphere as viewed by *STEREO-B*. Therefore, the event was observed from the two nearly perpendicular perspectives of *SDO* and *STEREO-B*. We examine full-disk 304 Å taken by the Extreme Ultraviolet Imager (EUVI; Wuelser et al. 2004; Howard et al. 2008) telescope aboard *STEREO-B*, with a pixel resolution of 1.″6 and a cadence of 10 minutes. To identify the associated CME, observations from inner coronagraphs (COR1; Thompson et al. 2010) aboard *STEREO-B* are also used. Having a field of view from 1.5 $R_\odot$ to 4 $R_\odot$, COR1 images were available at a 5 minute cadence.

3. RESULTS

The general evolution of the filament is shown in Figure 1. In Figures 1(a) and (b), two magnetograms are separated by 14 hr. The AIA 304 Å image (Figure 1(c)) obtained at the same time with the second magnetogram shows the filament at 01:28 UT just prior to its disturbance. From the location of the outlines of the filament, indicated by the red line on the magnetogram, we can find the filament anchored in the negative flux at its western endpoints and deduce that the filament is a sinistral one. Moreover, the two magnetograms show apparent cancellation of the field between the two times (see the area enclosed by the dashed circles in Figures 1(a) and (b)). This cancellation is mainly located under the middle segment of the filament and around the neutral line. Starting from about 01:38 UT, the filament rose upward slowly (Figures 1(d)–(f)). As shown in the AIA 94 Å image (see insets of Figures 1(d)–(f)), the post-event arcade started to form at about 01:58 UT. After 02:08 UT, the eruption starts to clearly exhibit a kink structure and bright front, as observed from the AIA 211 Å running difference images (Figures 1(g)–(i)). From the apparent clockwise rotation of the post-event loops' orientation (see the AIA 94 Å image in the insets of Figures 1(g)–(i)), we conclude that the overlying arcade has right-handed helicity. The composite images of *STEREO-B* EUVI 304 Å images with COR1 images are shown in Figures 1(j)–(l), in which the eruptive filament evolved into a CME. The red dashed lines in Figures 1(j)–(l) are connecting the centroid of the pre-eruptive filament (highlighted by the thick red lines) with the solar center, representing the radial direction of the pre-eruptive filament. However, the lifting filament and the associated CME did not propagate along that direction, but shifted northward. Therefore, the eruption underwent an obvious non-radial motion.

Although 12 s cadence *SDO* images are available, the EUV observation from *STEREO* determines that we can only obtain a pair of simultaneous 304 Å pictures from the two views every 10 minutes. We choose five moments to investigate the 3D structure of the filament by means of simultaneous observations. These moments include 01:26 UT, 01:46 UT, 02:06 UT, 02:16 UT, and 02:26 UT, covering the critical times during the filament evolution in the eruption. In this study, we used *scc_measure.pro* to reconstruct the filament. This procedure was first used to study the 3D trajectory of a comet (Thompson 2009) and has been widely used to analyze the structure of eruptive filaments (e.g., Bemporad 2009; Thompson 2011; Panasenco et al. 2011; Bi et al. 2011; Li et al. 2011; Zuccarello et al. 2012; Shen et al. 2012). It works on the basis of the "epipolar constraint" (Inhester 2006), which says that if a point appeared on an image from a certain view, it can only be located on a named epipolar line from another view. After obtaining the location of a point character on the two images from different views, we can identify the coordinates at this point in space.

On the 304 Å images from *SDO* and *STEREO-B* in Figure 2, the "+" symbols mark the points chosen to be reconstructed, with the error bars representing the width of the filament in the corresponding image. Interpolating enough points by using a cubic spline among the coordinates of the reconstructed points, we obtain some 3D curves that represent the filament axis at

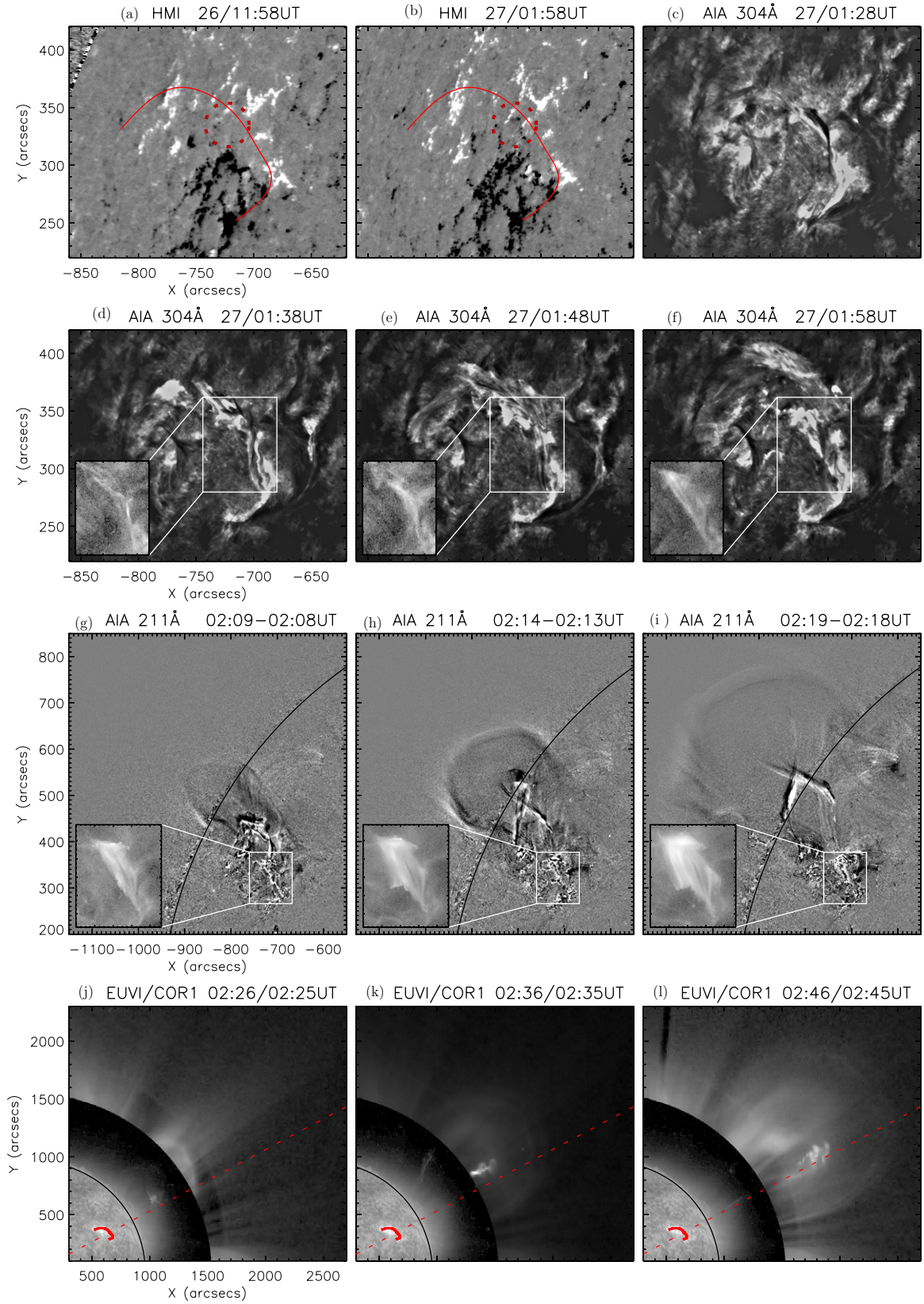

Figure 1. General evolution of the erupting region in HMI magnetograms ((a) and (b)), *SDO* AIA 304 Å images (c)–(f), *SDO* AIA 211 Å running difference images (g)–(i), and composite images of *STEREO-B* EUVI 304 Å images with COR1 images (j)–(l). In ((a) and (b)), the solid lines outline the axis of the pre-eruptive filament in AIA 304 Å ((g)–(i)), and the dashed circles mark the region showing the character of the flux cancellation. The insets in (d)–(i) are enlarged AIA 94 Å images of the area indicated by the dark boxes. The solid curves in (j)–(l) mark the axis of the pre-eruptive filament seen from the *STEREO-B* EUVI 304 Å, and the dashed lines indicate the radial direction of the centroid of the axis.

(A color version of this figure is available in the online journal.)

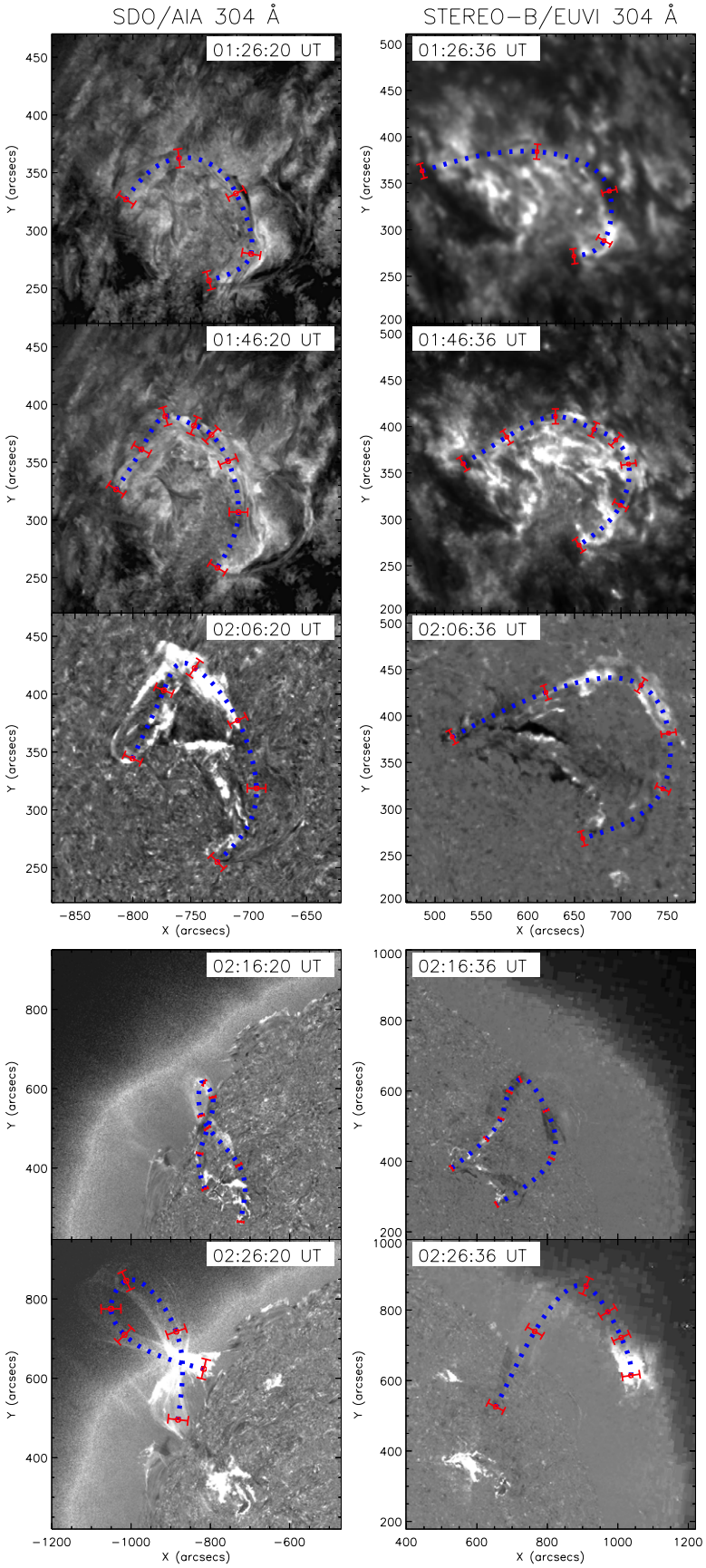

Figure 2. Erupting filament seen in 304 Å images from *SDO*/AIA 304 Å and *STEREO-B* EUVI 304 Å. The first two rows show the corresponding direct image, and the last three rows show the fixed-base difference images. The features used for reconstruction are marked by the small red circles along the filament axis, with the error bars representing the width of the filament in the corresponding image. Blue dashed lines indicate the reconstructed filament axis, which is determined by a cubic spline interpolation among the reconstruction features.

(A color version of this figure is available in the online journal.)

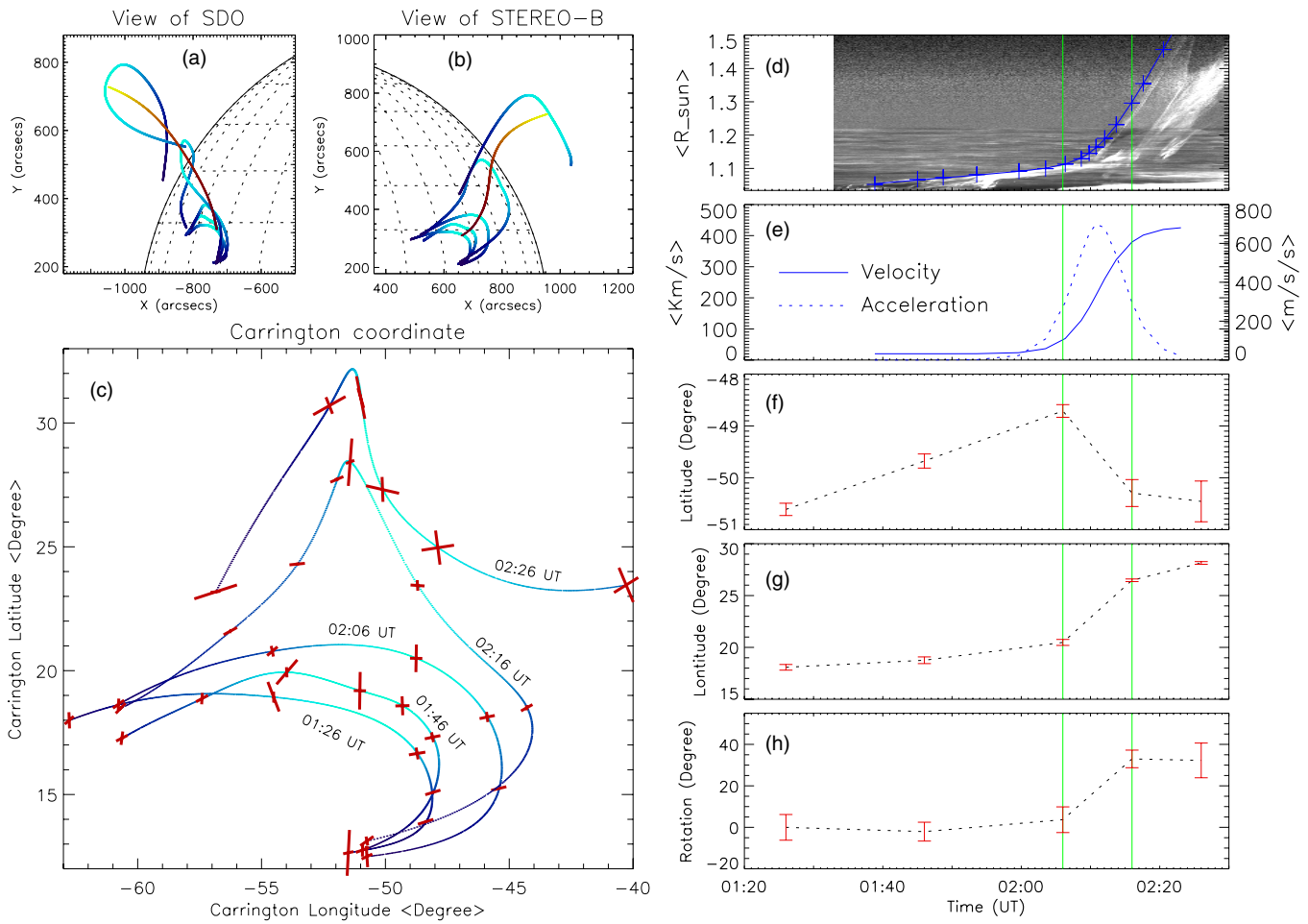

Figure 3. (a)–(c) Reconstructions based on the views of *SDO*, *STEREO-B*, and the Carrington coordinate. The blue curves with varying color depth indicate the shape of the reconstruction filament axis; darker/lighter blue indicates the lower/higher height. With the top at the height of 1.04, 1.07, 1.1, 1.25, and 1.65 $R_{\odot}$, the reconstructions are obtained at 01:26, 01:46, 02:06, 02:16, and 02:26 UT, respectively. The red curves are obtained by interpolation along the top of the reconstruction filament, and they then represent the trajectory of the rising filament. Similarly, the color depth indicates the height; darker/lighter red indicates lower/higher height. (d) Slit image composed of strips cut from the AIA 304 Å images through the trajectory as the red curve shows in (a). The asterisks match the brightening patterns on the image, representing the height-time data associated with the lifting filament, based on which the velocity and the acceleration are fitted by adopting a cosh function described in Sheeley et al. (2007). (e) Fitting velocity and the acceleration. (f)–(h) Variation of the latitude and the longitude of the filament top and the rotation angle at different times determined from the reconstructions. Two vertical green lines in (d)–(h) are located at 02:06 UT and 02:16 UT, during which the eruption was in the main acceleration phase.

(A color version of this figure is available in the online journal.)

every moment. The dashed lines in Figure 2 show the projection of these curves on both the *SDO* and *STEREO-B* images. We can see that the dashed lines match well with the observed filament axis at 304 Å from both views. Thus, we are confident that the interpolated curves represent the shape of the eruptive filament.

To clearly see the results of the reconstruction, we exhibit them from the views of *SDO* and *STEREO-B* in Figures 3(a) and (b), respectively. The blue curves with varying color depth indicate the shape of the reconstruction filament axis; darker/lighter blue indicates lower/higher height. The trajectory of the lifting filament is outlined by the red line in Figures 3(a) and (b), which consists of a group of points obtained by interpolation along the top of the reconstruction filament. Similarly, the color depth indicates the height. Consider that *SDO* provides higher cadence EUV images; we present a time slice of AIA 304 images in Figure 3(d) to detail the evolution of the filament. This slit image is composed of strips cut from the AIA 304 Å images through the trajectory, as the red curve shows in Figure 3. Since we have determined that these points consisting of the 3D trajectory have equal space in height, the actual height of the apex of the rising filament can be estimated from the brightening patterns in the time slice. Matching the patterns, a group of points (indicated by the "+" symbol) thus represents the height–time data associated with the lifting filament.

To characterize the main acceleration phase of the ejection and compare it to the timing of the rotation of the filament, we derived velocity and acceleration profiles from the height–time data. To this end, we adopt a cosh function described in Sheeley et al. (2007) for a rising CME profile. This function can reproduce profiles ranging from approximately constant acceleration to impulsive acceleration (Patsourakos et al. 2010). The fitting velocity and the acceleration are shown in Figure 3(e), in which the acceleration profile (the dashed line) exhibits an impulsive nature. It indicates that the acceleration of the filament peaked at about 02:10 UT and that the main acceleration phase commenced around 02:06 UT and lasted for 10 minutes. Two vertical lines are located at 02:06 UT and 02:16 UT during which the eruption was in the main acceleration phase.

We display the reconstructions (blue lines with varying color depth) in the Carrington coordinate in Figure 3(c), from which the filament can be seen by an observer above the eruption site. We also show error bars which represent the geometrical reconstruction error when the uncertainty for the reconnection is assumed to be the widths of the filament shown in Figure 2. Since the reconstruction uncertainty of a single point along the 3D curve due to the finite width of the loop in an image lies within the area of a trapezoid (Inhester 2006), the error bars consist of two lines indicating the axes of the error trapezoid. In agreement with the non-radial motion of the eruption as observed from *SDO* and *STEREO*, this plot shows that the filament expands toward the north. Figures 3(f) and (g) show the time evolution of the longitude and latitude of the top of the structures, respectively. Uncertainties on these parameters are estimated by the uncertainty for the reconstruction. These plots show that the variation in the longitude is inconspicuous, and there is about a 10° offset of the filament latitude during the eruption. A significant deflection seems to occur in the acceleration phase, during which the variations of the filament latitude are up to 6°. However, after the main acceleration, no remarkable deflection was found when the filament further propagated with an approximately constant velocity. This indicates that the deflection did not just result from a linear non-radial propagation.

From the evolution of the reconstructed filament in the Carrington coordinate in Figure 3(c), we can also find that the top of the filament is rotated in a clockwise direction while rising. To estimate the evolution of the rotation angle, we determine a vector defined by the two points located at the same certain altitude along a 3D structure and then consider the angles between the vectors and the direction of the pre-eruption filament as the rotation angle of eruption at different times. The evolution of the rotation angle measured in the height of 0.8 times the maximum altitude is shown in Figure 3(h). Error bars in this plot are obtained when we consider the geometrical reconstruction error and the variation of the measured height ranged within 0.1 times the maximum altitude. The plot clearly shows that the eruptive structure is rotated about 35° with respect to the pre-eruptive filament. From 01:26 UT to 02:06 UT, it is possible that some small rotation occurred, but the variation of the rotation angle is uncertain when we consider the geometrical errors. A significant rotation of the filament lasted about 10 minutes after 02:06 UT, when the top of the filament arrived at the height of 1.1 $R_\odot$. This indicates that, similar to the filament deflection in latitude, a significant rotation occurred mainly in the acceleration of the eruption, during which the filament rotates about 30°.

4. DISCUSSION AND INTERPRETATION

The filament experiences two distinct stages in terms of its rising speed: an initiation phase with a slow rise followed by a main acceleration phase. In the earlier initiation phase, the flux cancellation observed before the onset of the eruption may be a candidate for the mechanism triggering the eruption. Since flux convergence and cancellation have been shown to yield the formation of a flux rope through tether-cutting-like photospheric reconnection between previously sheared arcades, the reconnection in the lower corona might play a role in triggering the eruption of the filament by weakening its photospheric anchorage. Abundant examples from observations have shown that flux cancellation is favorable for the occurrence of the solar eruption (e.g., Wang & Shi 1993; Feynman & Martin 1995; Jiang et al. 2007; Sterling et al. 2007, 2011; Hong et al. 2011). On the other hand, since the result of the reconstructions cannot indicate the exact rotation angle in the initiation phase, it is uncertain whether kink instability triggered the eruption. After all, kink instability does not cause large rotation at an initial phase when the height is low.

At the main acceleration phase, the substantial rotation of the lifting filament is well observed. Such rotation of the sinistral filament eruption is consistent with the rotation–chirality relationship observed by Green et al. (2007) and the implications of flux-rope and sheared-arcade filament eruption models (e.g., Török et al. 2004; Lynch et al. 2009). As mentioned in Section 1, both the shear and the twist could contribute to the rotation of the filament (Isenberg & Forbes 2007). Although the twist in force-free flux ropes always causes at least some rotation, Kliem et al. (2012) suggested that the strength of the external shear field is the primary parameter determining the total rotation.

On the other hand, a remarkable characteristic of the eruption is that both the obvious rotation and the deflection toward the north are observed in the main acceleration phase. Since it is widely accepted that the non-radial motion of the eruption is strongly related to the large-scale coronal magnetic field, we place the event in the context of the global coronal field constructed by a potential-field source surface (PFSS; Schatten et al. 1969). In the PFSS model, the potential field matches a global radial magnetic field in the photosphere, which can be obtained by the observed line-of-sight magnetograms being assimilated into a flux-dispersal model (Schrijver & De Rosa 2003). To include more accurate information where the observed data are available, we use the global radial magnetic field inserted with the *SDO*/HMI magnetogram at 02:00 UT as the bottom boundary for the PFSS model (Guo et al. 2012). In Figures 4(a) and (b), selected field lines from the modeled field are superimposed on the *SDO*/HMI magnetogram and the synoptic map, respectively. The yellow lines indicate the closed bipolar field extending beyond 1.1 $R_\odot$ and within 1.3 $R_\odot$, and open lines with negative polarity are coded brown. Indicating the reconstruction of the five moments, the thick blue lines are also superimposed in Figure 4. Hence, from Figures 4(a) and (b), we can compare the propagation of the filament with the PFSS-modeled field as follows: first, reconstructions of the first three moments (01:26, 01:46 and 02:06 UT) show that the filament initially lies in the southern flank of the bipolar arcade coded yellow and propagates toward the northwest. Note that the filament propagates under 1.1 $R_\odot$ during this period, suggesting that before 02:06 UT the filament should be located under the arcade coded yellow. Therefore, the non-radial evolution of the filament in the initiation phase aligned the top of the filament with the top of the overlying bipolar. The picture is very similar to the scenario for the over-and-out CMEs, in which the large arcades play a key role in laterally guiding the eruption from moving radially outward. Yang et al. (2012) suggested that the arcades not only provide the guiding action but also confine the eruption in the low corona to facilitate the buildup of sufficient internal twist in the flux rope for development of the kink instability (Fan & Gibson 2007). Second, selected field lines show that the arcade field overlying the pre-eruption filament is embedded in a pseudostreamer structure (Wang et al. 2007) that separates coronal holes of the same polarity. Because the X-point where the open and closed field domains intersect is located at relatively low heights in pseudostreamer, this configuration may tend to facilitate the escape of filaments (Liu & Hayashi 2006).

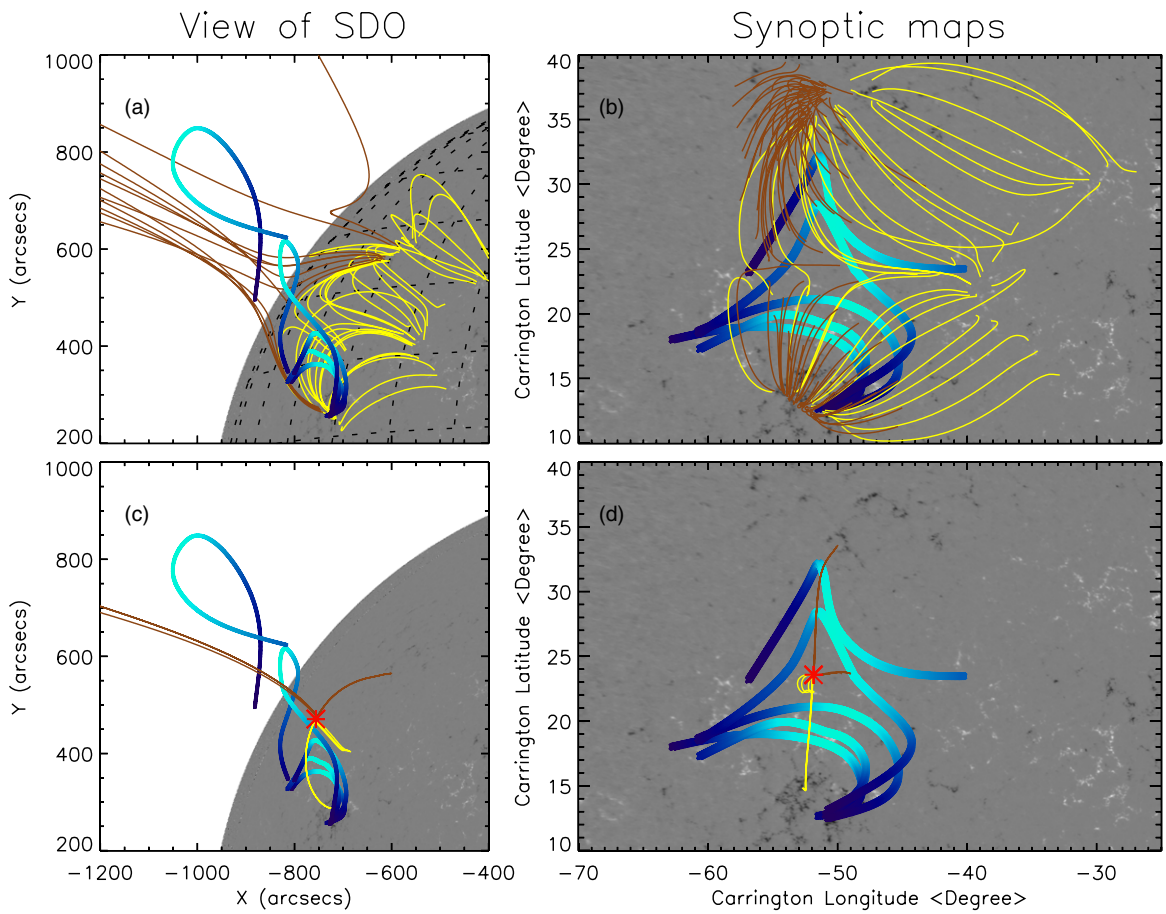

Figure 4. (a) and (c) *SDO*/HMI magnetogram at 02:00 UT. (b) and (c) *SDO*/HMI magnetogram at 02:00 UT transformed in the Carrington coordinates. In these panels, both the selected field line from the PFSS model and the reconstructions of the filament are superimposed. Closed field lines are coded in yellow if they extend beyond 1.1 $R_\odot$ and within 1.3 $R_\odot$; open field lines with negative polarity are coded in brown. The reconstructions are coded in blue with varying color depth; darker/lighter blue indicates the lower/higher height. With the top at a height of 1.04, 1.07, 1.1, 1.25, and 1.68 $R_\odot$, the reconstructions are obtained at 01:26, 01:46, 02:06 02:16, and 02:26 UT, respectively. The red asterisk in (c) and (d) marks a null point, which is determined using a trilinear method (Haynes & Parnell 2007) to model the PFSS field.

(A color version of this figure is available in the online journal.)

Using the trilinear null finding method of Haynes & Parnell (2007) to scan the PFSS-modeled field, we find a null point associated with the pseudostreamer, which is suited to the height of 1.10 $R_\odot$. We display the null point as a red asterisk in the *SDO* view and the Carrington coordinates in Figures 4(c) and (d), respectively, in which the field line traced from the neighborhood around the null point and the reconstructions is also shown. From Figure 4(c), we see that the null point is located above the reconstructed filament at 02:06 UT, while the null point appears to the northeast of the filament at 02:06 UT as seen from the Carrington coordinates in Figure 4(d). When the filament reaches the height of 1.25 $R_\odot$ at 02:16 UT, we see that the eastern segment of the filament is dragged toward north, but the western segment propagates with less deflection. Therefore, it seems that the significant deflection was related to the null point close to the eastern end of the filament, since the interchange reconnection is expected to occur in the null point inside the pseudostreamer when the filament propagates rapidly and approaches the null point, then the magnetic pressure imbalance due to the magnetic reconnection rapidly deflects the filament (Zuccarello et al. 2012). Moreover, the location of the null point implies that the reconnection would occur in the northern part of the eastern segment of the filament, and so the action of the deflection would mainly exert in the eastern part of the eruption. Thus, the asymmetric deflection indicated by the result of the 3D reconstruction further supports that the deflection is due to reconnection at the null point.

More importantly, the asymmetric deflection gives us an impression that an eruption will appear to be rotated when it is deflected asymmetrically in a different part, such as if one part is deflected more significantly than another. Furthermore, since the rotation of the filament was nearly simultaneous with the deflection in this event, both the rotation and the deflection might be indeed result from the same physical mechanism. Hence, we suggest that the action of the deflection is an alternative mechanism for the rotation in this event. In this scenario, the eruption is rotated by an external torque, which appears once one part of the eruption is dragged toward one side.

In all cases of the rotation of the eruptive filament recognized to date, there has been a one-to-one relationship between the helicity of the filament and the direction of the rotation, with filaments with positive helicity always rotating clockwise. This relationship also holds for the event described in this paper. Therefore, a natural question is raised: If asymmetric deflection is responsible for the rotation, might this relationship be a happenstance association, since the imbalance between the eruption and the large-scale corona field may lead to a torque with an arbitrary direction for a filament with a certain

helicity? Given that a filament exerts an external torque in the direction opposite to which that the filament helicity indicated (i.e., a filament having positive (negative) helicity is forced to rotate counterclockwise (clockwise) by an external torque) the rotation of the filament forced by the torque would imply that the writhe converts the twist into the eruptive filament. To our knowledge, however, this case has never been observed. In this hypothetical case, we speculate that the magnetic tension due to the twist field in the filament is very possibly playing a role in resisting the rotation. This means that only external torque in a direction consistent with that of the filament helicity can efficiently facilitate the filament rotation. Clearly, further studies on different types of 3D field configurations are necessary before we can understand the significance of the rotation due to the external torque associated with the large-scale field.

The authors are grateful to the anonymous referee for detailed comments and useful suggestions, which were crucial in improving the manuscript. The AIA and HMI data used here are courtesy of *SDO* (NASA) and the AIA/HMI consortia. The EUVI data are courtesy of *STEREO* and the SECCHI consortium. We thank the AIA, HMI, and SECCHI teams for facilitating easy access to calibrated data. This work is supported by the 973 Program (2011CB811403), by the Natural Science Foundation of China under grants 11173038 and 11273056, and by the CAS grant KJCX2-EW-T07.

REFERENCES

Bemporad, A. 2009, ApJ, 701, 298
Bemporad, A., Mierla, M., & Tripathi, D. 2011, A&A, 531, A147
Bemporad, A., Sterling, A. C., Moore, R. L., & Poletto, G. 2005, ApJL, 635, L189
Berger, M. A., & Prior, C. 2006, JPhA, 39, 8321
Bi, Y., Jiang, Y., Yang, L., et al. 2011, NewA, 16, 276
Boerner, P., Edwards, C., Lemen, J., et al. 2012, SoPh, 275, 41
Cheng, X., Ding, M. D., & Zhang, J. 2010, ApJ, 712, 1302
Cohen, O., Attrill, G. D. R., Schwadron, N. A., et al. 2010, JGRA, 115, 10104
Démoulin, P., & Aulanier, G. 2010, ApJ, 718, 1388
Fan, Y. 2005, ApJ, 630, 543
Fan, Y., & Gibson, S. E. 2007, ApJ, 668, 1232
Feynman, J., & Martin, S. F. 1995, JGR, 100, 3355
Filippov, B. P., Gopalswamy, N., & Lozhechkin, A. V. 2001, SoPh, 203, 119
Forbes, T. G., & Isenberg, P. A. 1991, ApJ, 373, 294
Green, L. M., Kliem, B., Török, T., van Driel-Gesztelyi, L., & Attrill, G. D. R. 2007, SoPh, 246, 365
Guo, Y., Ding, M. D., Liu, Y., et al. 2012, ApJ, 760, 47
Haynes, A. L., & Parnell, C. E. 2007, PhPl, 14, 082107
Hong, J., Jiang, Y., Zheng, R., et al. 2011, ApJL, 738, L20
Hood, A. W. 1992, PPCF, 34, 411
Hood, A. W., & Priest, E. R. 1979, SoPh, 64, 303
Howard, R. A., Moses, J. D., Vourlidas, A., et al. 2008, SSRv, 136, 67
Inhester, B. 2006, arXiv:astro-ph/0612649
Isenberg, P. A., & Forbes, T. G. 2007, ApJ, 670, 1453
Jacobs, C., Roussev, I. I., Lugaz, N., & Poedts, S. 2009, ApJL, 695, L171
Ji, H., Wang, H., Schmahl, E. J., Moon, Y.-J., & Jiang, Y. 2003, ApJL, 595, L135
Jiang, Y., Yang, J., Zheng, R., Bi, Y., & Yang, X. 2009, ApJ, 693, 1851
Jiang, Y.-C., Shen, Y.-D., & Wang, J.-X. 2007, ChJAA, 7, 129
Joshi, A. D., & Srivastava, N. 2011, ApJ, 730, 104
Kliem, B., Titov, V. S., & Török, T. 2004, A&A, 413, L23
Kliem, B., & Török, T. 2006, PhRvL, 96, 255002
Kliem, B., Török, T., & Thompson, W. T. 2012, SoPh, 281, 137
Li, T., Zhang, J., Zhang, Y., & Yang, S. 2011, ApJ, 739, 43
Liu, R., Gilbert, H. R., Alexander, D., & Su, Y. 2008, ApJ, 680, 1508
Liu, Y. 2008, ApJL, 679, L151
Liu, Y., & Hayashi, K. 2006, ApJ, 640, 1135
Lugaz, N., Downs, C., Shibata, K., et al. 2011, ApJ, 738, 127
Lynch, B. J., Antiochos, S. K., Li, Y., Luhmann, J. G., & DeVore, C. R. 2009, ApJ, 697, 1918
Moore, R. L., & Sterling, A. C. 2007, ApJ, 661, 543
Panasenco, O., Martin, S., Joshi, A. D., & Srivastava, N. 2011, JASTP, 73, 1129
Patsourakos, S., Vourlidas, A., & Kliem, B. 2010, A&A, 522, A100
Rust, D. M., & LaBonte, B. J. 2005, ApJL, 622, L69
Schatten, K. H., Wilcox, J. M., & Ness, N. F. 1969, SoPh, 6, 442
Schrijver, C. J., & De Rosa, M. L. 2003, SoPh, 212, 165
Sheeley, N. R., Jr., Warren, H. P., & Wang, Y.-M. 2007, ApJ, 671, 926
Shen, C., Wang, Y., Gui, B., Ye, P., & Wang, S. 2011a, SoPh, 269, 389
Shen, Y., Liu, Y., & Su, J. 2012, ApJ, 750, 12
Shen, Y.-D., Liu, Y., & Liu, R. 2011b, RAA, 11, 594
Sterling, A. C., Harra, L. K., & Moore, R. L. 2007, ApJ, 669, 1359
Sterling, A. C., Moore, R. L., & Freeland, S. L. 2011, ApJL, 731, L3
Sun, X., Hoeksema, T., Liu, Y., Chen, Q., & Hayashi, K. 2012, ApJ, 757, 149
Thompson, W. T. 2009, Icar, 200, 351
Thompson, W. T. 2011, JASTP, 73, 1138
Thompson, W. T., Kliem, B., & Török, T. 2012, SoPh, 276, 241
Thompson, W. T., Wei, K., Burkepile, J. T., Davila, J. M., & St. Cyr, O. C. 2010, SoPh, 262, 213
Török, T., Berger, M. A., & Kliem, B. 2010, A&A, 516, A49
Török, T., & Kliem, B. 2005, ApJL, 630, L97
Török, T., Kliem, B., & Titov, V. S. 2004, A&A, 413, L27
Wachter, R., Schou, J., Rabello-Soares, M. C., et al. 2012, SoPh, 275, 261
Wang, J., & Shi, Z. 1993, SoPh, 143, 119
Wang, Y.-M., Sheeley, N. R., Jr., & Rich, N. B. 2007, ApJ, 658, 1340
Wuelser, J.-P., Lemen, J. R., Tarbell, T. D., et al. 2004, Proc. SPIE, 5171, 111
Yang, J., Jiang, Y., Bi, Y., et al. 2012, ApJ, 749, 12
Zhang, J., Dere, K. P., Howard, R. A., & Vourlidas, A. 2004, ApJ, 604, 420
Zhang, J., Wang, J., Deng, Y., & Wu, D. 2001, ApJL, 548, L99
Zhou, G. P., Wang, J. X., Zhang, J., et al. 2006, ApJ, 651, 1238
Zuccarello, F. P., Bemporad, A., Jacobs, C., et al. 2012, ApJ, 744, 66